Spatial–spectral method for classification of hyperspectral images

Xiaoyong Bian,[1,2,*] Tianxu Zhang,[1] Luxin Yan,[1] Xiaolong Zhang,[2] Houzhang Fang,[1] and Hai Liu[1]

[1]*Science and Technology on Multi-spectral Information Processing Laboratory, Institute for Pattern Recognition and Artificial Intelligence, Huazhong University of Science and Technology, Wuhan, Hubei 430074, China*

[2]*School of Computer Science and Technology, Wuhan University of Science and Technology, Wuhan, Hubei 430081, China*

**Corresponding author: xyjconf10@163.com*

Received October 16, 2012; revised January 27, 2013; accepted January 28, 2013; posted February 1, 2013 (Doc. ID 178083); published March 5, 2013

Spatial–spectral approach with spatially adaptive classification of hyperspectral images is proposed. The rotation-invariant spatial texture information for each object is exploited and incorporated into the classifier by using the modified local Gabor binary pattern to distinguish different types of classes of interest. The proposed method can effectively suppress anisotropic texture in spatially separate classes as well as improve the discrimination among classes. Moreover, it becomes more robust with the within-class variation. Experimental results on the classification of three real hyperspectral remote sensing images demonstrate the effectiveness of the proposed approach. © 2013 Optical Society of America

OCIS codes: 100.3008, 100.4145, 100.5760, 330.6100, 330.6180.

Hyperspectral remote sensing (HRS) images consist of hundreds of spectral bands spanning the visible and infrared spectrum [1] that typically cover a spectral range of 0.4–2.5 μm, with 210–224 spectral bands and a spatial resolution of 3–20 m per pixel. In past decades, many different techniques were presented in the extensive literature for the classification of HRS images, ranging from generative methods to discriminative classifiers based on trained models. For example, Polarization-based [2] and support vector machine (SVM) [3,4] methods have been used. The gray-level co-occurrence matrix (GLCM) is a popular statistical procedure for analyzing texture that is successful in the analysis of remote sensing data. In [5], Huang *et al.* extracted structural features of a direction-lines histogram for the classification of urban areas from high-spatial-resolution imagery. Recently some spatial classification methods were developed for land-cover types in HRS imagery [6,7]. However, these methods maintain a limited capacity in challenging classification scenarios.

Exploiting spatial information shows that global and local properties of an image (patch) can improve land-cover classification of HRS data [8]. Gabor and local binary pattern (LBP) were fused and successfully applied in face recognition. Tan and Triggs [9] extracted Gabor and LBP feature sets for face recognition, and these features seemed to be more complementary than might have been expected. Zhang *et al.* [10] proposed a local Gabor binary pattern histogram sequence to represent face information that gained a high recognition rate. To the best of our knowledge, no work concentrated on LGBP features for classification of HRS data has been reported.

Considering the case where a land-cover class in HRS data is anisotropically distributed, anisotropic texture features from a spatially separate class are obtained via Gabor filters. However, a direct Gabor-based classification method may confuse this class and other classes because of inaccurate texture representation for the spatially separate class. To overcome the shortcomings, we propose a modified LGBP (MLGBP) measure to automatically extract spatial features for each central pixel of interest in a local neighborhood, and SVM is employed to process the spatial–spectral features in the classification of HRS imagery. Consequently, MLGBP can effectively suppress orientation textures of spatially localized classes as well as improve discrimination among classes. Moreover, MLGBP becomes more robust with respect to the within-class variation.

MLGBP characterizes LGBP with a rotation-invariant-uniform operator, and represents the homogeneity measurement between the central pixel and its neighboring pixels for summarizing local gray-level structure [11], defined as

$$\mathrm{MLGBP} = \begin{cases} \min\left\{\mathrm{ROR}\left(\sum_{p=0}^{P-1} s(g_i - g_c)2^p, i\right) | i = 0, 1, \cdots, P-1\right\} & \text{if } U(\mathrm{LBP}_{P,R}) \le 2 \\ P+1 & \text{otherwise} \end{cases}, \tag{1}$$

$$U(\mathrm{LBP}_{P,R}) = |s(g_{P-1} - g_c) - s(g_0 - g_c)| + \left|\sum_{i=1}^{P-1} s(g_i - g_c) - s(g_{P-1} - g_c)\right|, \tag{2}$$

where P, R denote the number of points and the radius of a circle based on a circularly symmetric neighbor set of

 © 2013 Optical Society of America

central pixel g_c and surrounding pixels $(g_i)_{i=0}^{P-1}$, whereas $U(\cdot)$ defines the frequency of 0-1 and 1-0 transition in a circular bit string given a pattern $\mathrm{LBP}_{P,R}$, and a "uniform" pattern means it contains at most two transitions. Meanwhile, $s(x)$ takes 1 if $x \geq 0$ and 0 otherwise. $\mathrm{ROR}(x, i)$ indicates the operation of rotating right i bits on x, and $\min(\cdot)$ takes the minimum value from input value sets. It is noted that the macrostructure and microstructure of objects are detected by the proposed approach, i.e., multiscale and multiorientation Gabor-based rotation-invariant-uniform LBP. The count of rotation-invariant-uniform LBP occurrence is calculated to estimate the underlying distribution by the histogram. In this way, a connection between global and local structures is built. The inspiration comes from the exploitation of spatial feature sets in a hyperspectral urban area [5,8]. An illustration of spatial–spectral feature histograms for six land-cover types is shown in Fig. 1.

As can be seen from Fig. 1, only the spectral feature from the first three histograms on each plot is inadequate for classification of HRS images. However, the spatial features from the latter 10 histograms extracted from a ground patch of the given class on each plot can achieve different characteristics for different classes. Hence, the use of these measures will provide additional discriminatory information in classification.

Summarizing, two good features of MLGBP can be drawn: (1) for the spatially separate classes, the rotation-invariant-uniform LBP operator is enforced to spatially suppress anisotropic texture difference; (2) for large within-class variation, the invariance against gray-scale shifts is achieved by considering just the signs of the difference instead of their exact values in Eq. (2), and the histogram feature sets obtained by MLGBP still represent the most key information of the image (patch).

To demonstrate the performance of MLGBP, we carried out the classification of three real HRS images using extracted spatial and spectral features. The classifiers of K-nearest-neighbor (K-NN) [12], Gauss process maximum likelihood (GP-ML) [7], and SVM are employed for comparison. A one-against-all [4] classification scheme is adopted for the SVM classification, and a grid searching of fivefold cross validation is performed to obtain optimal regularization parameters C and Gauss kernel width σ. The configuration for MLGBP is the following: P, R parameters are tuned in the range $P = [8, 16, 32]$, $R = [1, 2, 3]$, respectively. Values of $P = 8$ and $R = 1$ exhibit the best performance in our experiments. Each set of ground surveys is randomly divided into a training set, a validation set, and a test set with 55%, 35%, and 10% sampling rates, respectively. All the experiments are performed using five random realizations of training sets. Two

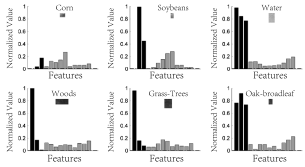


Fig. 1. Spectral and spatial features for different classes. All the features were normalized to [0,1]. From left to right on each plot: the first three spectral and the latter 10 spatial histogram features extracted by our method from each ground class.

evaluation metrics, overall accuracy (OA) and kappa statistics (kappa) from the confusion matrix for each realization are computed, and as the final result the average OA and kappa statistic on the five realizations are provided. Class-specific acuracies for both producer's accuracy (PA) and user's accuracy (UA) are also reported.

Three hyperspectral datasets for Indian Pines, Kennedy Space Center (KSC), and Botswana are used in experiments, with different sizes (145×145, 512×614, and 1476×256 pixels), different contexts (crop, vegetation areas), different spatial resolutions (20, 18, and 30 m per pixel, respectively), and different bands (220, 224, and 242 bands, respectively). Removal of water absorption and noisy bands resulted in 200, 176, and 145 bands, respectively. Different class labels of interest associated with each ground survey are {2, 3, 5, 6, 8, 10, 11, 12, 14}, {1, 2, 3, 4, 6, 8, 9, 10, 11, 12, 13}, and {1, 3, 5, 6, 7, 9, 10, 11, 13}, respectively. Specifically, owing to the presence of "difficult classes" with spectrally overlapping signatures in three hyperspectral datasets, these scenarios constitute very challenging classification problems. Three spectral bands (RGB) were obtained by principal component analysis (PCA) on each investigated HRS image.

(1) Comparison of RGB, GLCM, GLBP, and MLGBP: the texture features adopted on GLCM include contrast, entropy, homogeneity, angular second moment, and correlation [13]. These features are calculated setting the interpixel distance equal to 1 in all four directions and stacked. The high dimensions of extracted spatial feature sets are reduced via PCA and normalized prior to a classification analysis. An SVM classifier was used for this comparison. Their accuracies with different classes are provided in Table 1 and classification maps for all four feature sets on the Indian Pines test set are shown in Fig. 2; it is found that MLGBP achieves slightly higher accuracies than LGBP, GLCM, and the increases in OA

Table 1. Classification Accuracies in Percentages Except for Kappa by SVM for Different Feature Sets on Indian Pines Image[a]

%PA (%UA)	RGB	GLCM	LGBP	MLGBP
Corn-notill	51.0	95.47	95.88	**99.80**
	(60.65)	(94.05)	(97.34)	**(99.20)**
Corn-min	53.04	97.71	97.46	**100.0**
	(53.32)	(96.98)	(92.53)	**(100.0)**
Grass-pasture	87.72	**100.0**	98.25	**100.0**
	(24.63)	(75.0)	(83.58)	**(100.0)**
Grass-trees	94.14	**100.0**	**100.0**	**100.0**
	(87.05)	(96.85)	(96.24)	**(100.0)**
Hay-windrowed	97.96	**100.0**	**100.0**	**100.0**
	(90.57)	(94.23)	(98.0)	**(100.0)**
Soybeans-notill	78.22	96.59	98.49	**100.0**
	(58.42)	(88.24)	(99.24)	**(100.0)**
Soybeans-min	67.11	93.79	98.27	**99.21**
	(82.29)	(98.70)	(99.55)	**(99.95)**
Soybean-clean	63.22	99.43	98.85	**100.0**
	(22.22)	(96.11)	(96.63)	**(100.0)**
Woods	82.55	99.06	99.65	**100.0**
	(98.88)	(99.65)	**(100.0)**	**(100.0)**
% OA	68.56	96.16	98.14	**99.67**
Kappa	0.649	0.952	0.976	**0.996**

[a]UA are in brackets. The best results are highlighted in BOLD.

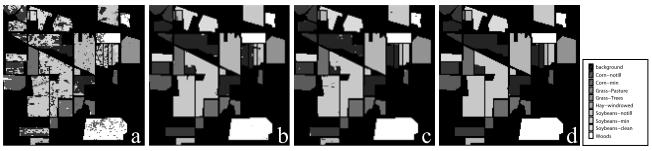


Fig. 2. Classification maps for different features on Indian Pines image. (a)–(d) Classification maps for RGB, GLCM, LGBP, and MLGBP features, respectively.

(kappa) are 1.53% (0.02) and 3.51% (0.04), respectively. Compared with RGB, the clear improvements for MLGBP in OA (kappa) are about 31.11% (0.35). The effectiveness of classification accuracies can be further confirmed by carefully visually checking the classification maps in Fig. 2. In Fig. 2(a), the obvious misclassifications among class corn-no till and soybeans (subclass: no till, min) illustrates the inadequacy of spectral classification of HRS data, which is greatly alleviated in Figs. 2(b) and 2(c), and the best result is achieved in Fig. 2(d). Therefore, the inclusion of spatial information in the classifier helps in the discrimination of land-cover classes.

(2) Comparison of K-NN, GP-ML, and SVM: for different classifiers, the performances versus four different feature sets for the Indian Pines image are plotted in Fig. 3, from which it is observed that the proposed MLGBP features give consistently better performance independent of the classifiers used.

In order to validate that the proposed algorithm of classification and spatial feature extraction works in a stable manner, two other HRS images are examined. The accuracies of different feature sets achieved by SVM for the KSC image are shown in Table 2.

As in the Indian Pines experiments, the proposed MLGBP performs better than LGBP, GLCM, and RGB features in a statistically meaningful fashion; the improvements for MLGBP in OA (kappa) are about 2.39% (0.03), 2.72% (0.03), and 10.97% (0.13), respectively, and almost all of the class-specific accuracies are improved. Thus, MLGBP shows good performance for the KSC image and can overcome their defects to some extent. The reason for this is the presence of different orientations of class distribution although the mixed pixels exist. Similar to the results in the previous images, average accuracy and kappa statistics for Botswana image are obtained, and hold for interpreting the consistency of proposed approach. Hence the results are not presented.

In conclusion, an improved spatial–spectral method with spatial adaptation is proposed. The proposed MLGBP method can achieve consistent improvements for different types of classes of interest according to the accuracies and classification maps in experiments. Moreover, it becomes more robust with respect to the within-class variation. SVM is more interpretable for the hybrid features.

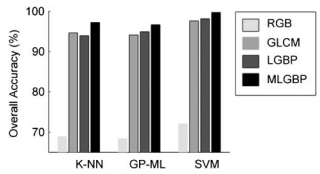


Fig. 3. Accuracy statistics for different classifiers versus different feature sets on Indian Pines image.

Table 2. Classification Accuracies in Percentages Except for Kappa by SVM for Different Feature Sets on KSC Image[a]

%PA (%UA)	RGB	GLCM	LGBP	MLGBP
Scrub	83.78	96.94	95.32	**100.0**
	(99.15)	**(100.0)**	**(100.0)**	**(100)**
Willow swamp	91.89	97.30	**100.0**	**100.0**
	(42.5)	(97.30)	(75.51)	**(100)**
CP hammock	92.0	98.0	98.0	**100.0**
	(93.88)	**(100.0)**	(92.45)	**(100)**
CP/Oak	76.09	**100.0**	91.30	**100.0**
	(72.92)	(97.87)	(87.5)	**(100)**
Oak/broadleaf	69.57	**100.0**	95.65	**100.0**
	(25.81)	(57.50)	(64.71)	**(100)**
Graminoid marsh	77.78	96.89	92.89	**100.0**
	(75.43)	(92.77)	(95.43)	**(100)**
Spartina marsh	90.13	93.63	98.09	**100.0**
	(90.42)	(96.71)	(97.47)	**(100)**
Cattail marsh	78.79	94.44	97.98	**100.0**
	(72.22)	(95.41)	(96.04)	**(100)**
Salt marsh	97.18	99.53	**100.0**	**100.0**
	(94.10)	(98.60)	(99.53)	**(100)**
Mud flats	83.50	95.96	97.98	**100.0**
	(91.85)	(95.64)	(98.98)	**(100)**
Water	99.86	99.59	**100.0**	**100.0**
	(100.0)	(99.72)	**(100.0)**	**(100)**
%OA	89.03	97.28	97.61	**100.0**
Kappa	0.873	0.968	0.972	**1.0**

[a]UA are in brackets. The best results are highlighted in BOLD.

This work was supported by the National Natural Science Foundation of China under grant nos. 60975031, 61273225, and 61227007.

References

1. R. Green, M. Eastwood, C. Sarture, T. Chrien, M. Aronsson, B. Chippendale, J. Faust, B. Pavri, C. Chovit, M. Solis, M. Olah, and O. Williams, Remote Sens. Environ. **65**, 227 (1998).
2. M. Hyde, J. Schmidt, M. Havrilla, and S. Cain, Opt. Lett. **35**, 21 (2010).
3. A. Filippi, R. Archibald, B. Bhaduri, and E. Bright, Opt. Express **17**, 23823 (2009).
4. X. Bian, T. Zhang, X. Zhang, L. Yan, and B. Li, Cogn. Comput. **4**, 2 (2012).
5. X. Huang, L. Zhang, and P. Li, IEEE Geosci. Remote Sens. Lett. **4**, 2 (2007).
6. Y. Tarabalka, M. Fauvel, J. Chanussot, and J. Benediktsson, IEEE Geosci. Remote Sens. Lett. **7**, 736 (2010).
7. G. Jun and J. Ghosh, IEEE Trans. Geosci. Remote Sens. **49**, 7 (2011).
8. F. Dell'Acqua, P. Gamba, A. Ferari, J. Palmason, J. Benediktsson, and K. Arnason, IEEE Geosci. Remote Sens. Lett. **1**, 4 (2004).
9. X. Tan and B. Triggs, in *International Workshop on Analysis and Modeling of Faces and Gestures* (Springer-Verlag, 2007), pp. 235–249.
10. W. Zhang, S. Shan, and W. Gao, in *IEEE International Conference on Computer Vision* (IEEE, 2005), pp. 786–791.
11. T. Ojala, M. Pietikainen, and T. Maenpaa, IEEE Trans. Pattern Anal. Machine Intell. **24**, 7 (2002).
12. H. Zhang, A. Berg, M. Maire, and J. Malik, in *IEEE International Conference on Computer Vision and Pattern Recognition* (IEEE, 2006), pp. 2126–2136.
13. Y. Zhang, ISPRS J. Photogramm. Remote Sens. **54**, 1 (1999).